Electronic and optical properties of novel carbon allotropes

Zhanyu Wang[a], F. Dong [a], B. Shen [a], R. J. Zhang[a], Y. X. Zheng[a], L.Y. Chen[a], S.Y. Wang[a,b,c,*], C. Z. Wang[c], K. M. Ho[c], Yuan-Jia Fan[d], Bih-Yaw Jin[d] and Wan-Sheng Su[e,*]

[a]*Shanghai Ultra-Precision Optical Manufacturing Engineering Center and Department of Optical Science and Engineering, Fudan University, Shanghai, 200433, China*

[b]*Key Laboratory for Information Science of Electromagnetic Waves (MoE), Shanghai 200433, China*

[c]*Ames Laboratory, U. S. Department of Energy and Department of Physics and Astronomy, Iowa State University, Ames, Iowa 50011, USA*

[d]*Department of Chemistry, National Taiwan University, Taipei 10617, Taiwan*

[e]*National Center for High-Performance Computing, Hsinchu 30076, Taiwan and Department of Physics, National Chung Hsing University, Taichung 40227, Taiwan*

[*]Corresponding authors. Fax: +86 021 65643422, Tel: +86 021 65642970, E-mail address: songyouwang@fudan.edu.cn (S. Y. Wang); and Fax: +886 3 5776082, Tel: +886 3 5776085 ext. 290, E-mail address: wssu@nchc.narl.org.tw (Wan-Sheng Su).

Abstract

The vibrational properties, electronic structures and optical properties of novel carbon allotropes, such as monolayer penta-graphene (PG), double-layer PG and T12-carbon, were studied by first-principles calculations. Results of phonon calculations demonstrate that these exotic carbon allotropes are dynamically stable. The bulk T12 phase is an indirect-gap semiconductor having a quasiparticle (QP) bandgap of ~5.19 eV. When the bulk material transforms to a 2D phases, the monolayer and double-layer PG become quasi-direct gap semiconductors with smaller QP band gaps of ~4.48 eV and~3.67 eV, respectively. Furthermore, the partial charge density analysis indicates that the 2D phases retain part of the electronic characteristics of the T12 phase. The linear photon energy-dependent dielectric functions and related optical properties including refractive index, extinction coefficient, absorption spectrum, reflectivity, and energy loss spectrum were also computed and discussed. Additionally, the chemical stability of monolayer PG and the electronic and optical properties of double-side hydrogenated monolayer PG were also studied. The results obtained from our calculations are beneficial to practical applications of these exotic carbon allotropes in optoelectronics and electronics.

1. Introduction

Recently, two-dimensional (2D) nanomaterials have attracted considerable experimental and theoretical interests due to the surge in graphene research [1-7] which opens an avenue for the development of 2D semiconducting materials for future multifunctional optoelectronic device applications. Many 2D materials exhibiting a variety of extraordinary properties have being explored and designed [8-14]. Because of their atomic scale thickness, the existence of quantum confinements, and other unique planar advantages, 2D materials are attractive for use in low-power, smaller, more flexible, and more efficient next-generation nanoelectronic devices, as well as for catalysis, sensing, and energy storage applications [15-20]. The unique physical and chemical properties of 2D materials are intimately related to their atomic arrangement. Most of the graphene-like 2D materials consist of hexagonal lattice and in some cases are accompanied by carbon pentagons and heptagons. [1, 21] More new class of 2D materials comprised of a different topological arrangement of atoms and novel properties are desirable to provide the broadest offering available to meet virtually every application.

Following the discovery of graphene, penta-graphene (PG) [1], which is entirely composed of carbon pentagons, was predicted and reported. As depicted in Fig. 1a, monolayer PG (MPG), which consists of a packed layer of 4-coordinated C atoms (C1) sandwiched between two layers of 3-coordinated C atoms (C2), has a thickness of ~1.2 Å. The molecular dynamics simulations [1] indicate that hydrogen intercalation may be a viable way to selectively break the interlayer C-C bonds in T12-carbon (TC) and to chemically exfoliate a PG monolayer. Furthermore, the bulk T12-carbon may be synthesized experimentally via decompression from the appropriate high-pressure phase [22]. Meanwhile, the structural properties, and the electronic and phonon band structures of monolayer PG and T12-carbon were also studied in some literatures [1, 13, 14, 22-24]. For example, thorough and systematic theoretical calculations have been performed to confirm that the monolayer PG and T12-carbon are dynamically and mechanically stable. And the monolayer PG with a large intrinsic quasi-direct bandgap [1] of ~3.48 eV is a desirable candidate for optoelectronics and digital electronics. Equally important, physical properties such as energy gap, bulk modulus, shear modulus, and Vickers hardness of T12-carbon resemble those of diamond phases. Interestingly, the basic characteristics of monolayer PG can be tailored by stacking to form 2D materials, rolling to form 1D

nanotubes, and even wrapping to form 0D C_{20} fullerenes [25]. These versatile carbon allotropes are expected to offer opportunities for broad applications in nanoelectronics and optical devices. In order to take full advantage of the properties of these novel materials for eventual technological applications, a better understanding of their electronic structure and optical properties is required.

In this work, we employ first-principles calculations to investigate the structural, electronic, and optical properties of monolayer PG, AB stacked double-layer PG (DPG) and T12-carbon. Additionally, the chemical stability of monolayer PG and the electronic, and optical properties of double-side hydrogenated monolayer PG are also discussed. The paper is organized as follows: in Section 2, the computational techniques adopted in this study are described in detail. Results and discussion of the structural, vibrational, electronic, and optical properties as well as the chemical stability are presented in Section 3. Finally, conclusions are given in Section 4.

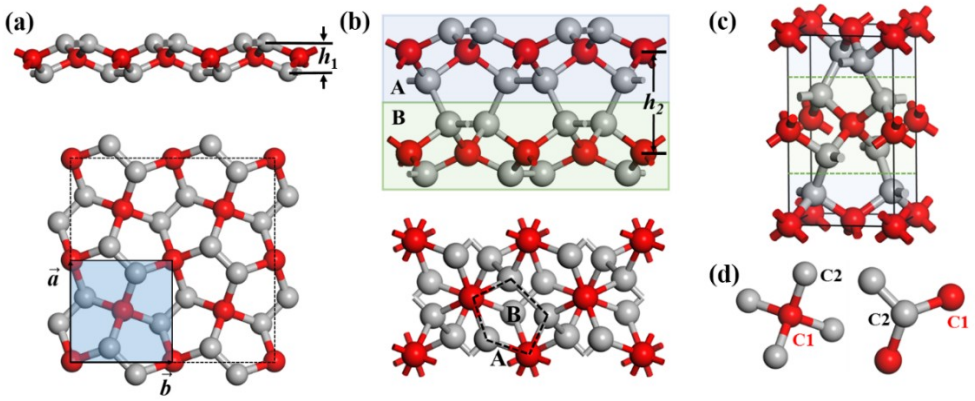

Fig. 1- Side and top views of atomic structure for (a) monolayer PG and (b) AB stacked double-layer PG. Figure 1(a) shows a 2×2 supercell, and the primitive unit cell with lattice vectors is highlighted by a parallelogram. Figure (b) shows that C2 atoms in layer B are located on the hollow sites of layer A. (c) The crystal structure of T12-carbon. (d) Coordination environment of C1 and C2 atoms for monolayer PG.

2. Computational details

The total energy and the Hellmann-Feynman force calculations were carried out using the density functional theory (DFT), implemented in the Vienna *ab initio* simulation package (VASP) [26-28]. The projector-augmented wave function (PAW) method [29] with the Perdew-Burke-Ernzerh (PBE) [30] of generalized gradient approximation (GGA) was applied. The 2D slabs are separated by a vacuum distance of ~15 Å in the perpendicular direction. The plane-wave energy cutoff was 500 eV. The

Brillouin-zone (BZ) was sampled by 9×9×1 (MPG and DPG) and 9×9×5 (TC) Monkhorst-Pack [31] k meshes for the primitive unit cells. The total energy was calculated with high precision, converged to 10^{-6} eV/atom and the lattice constants and the atom coordinates were optimized until the interatomic forces were less than 10^{-2} eV/Å.

The phonon calculations were performed using the supercell method through the PHONOPY code [32], and the real-space force constants of supercells were calculated through the density-functional perturbation theory (DFPT) as implemented in VASP. For our phonon calculations, necessary routine numerical checks on the reliability of the supercell size were made. Supercells containing 4×4×1 primitive cells were used for monolayer and double-layer PG, and a 4×4×2 one was used for T12-carbon.

For all the carbon allotropes, the hybrid HSE06 functional [33, 34] was used for electronic structural computations. For comparison purposes, the GW calculations were also performed in a partially self-consistent way (the so-called GW_0 approach) [35]. The PBE wave functions were used as a starting point for the GW_0 calculations. To achieve numerical accuracy in GW_0 calculations, the number of virtual orbitals was chosen to be 3 times greater than the number of occupied bands. The energy cutoff for the response functions was set to be at least 150 eV, and the obtained band gap is essentially the same if a higher cutoff of 200 eV is used. For visualization purposes, the GW_0 band structures were interpolated to a finer grid using the approach of maximally localized Wannier functions [36]. The dielectric function was obtained by solving the BSE on top of the GW results. The BSE calculations were performed by using the eight highest valence bands and eight lowest conduction bands of each phase. Furthermore, all other optical constants of energy dependence, those of refractive index, extinction coefficient, absorption spectrum, reflectivity, and energy loss spectrum can be derived from $\varepsilon_1(\omega)$ and $\varepsilon_2(\omega)$.

For simulations of H_2 dissociation and H diffusion, a 2×2×1 supercell and the 4×4×1 mesh of k-points were used. In order to determine the minimum energy path (MEP), we used the climbing image nudged elastic band (CI-NEB) method [37, 38]. Different number of images between the initial and finial configurations were chosen to ensure a good determination of the MEP for the dissociation and diffusion paths. The activation barrier E_a is defined as the energy difference between the initial state

(IS) and the saddle point. The energy of single molecular hydrogen adsorption is defined to be

$$E_{ads} = E_{tot}(\mathrm{PG+H_2}) - E_{tot}(\mathrm{PG}) - E_{tot}(\mathrm{H_2}),$$

where $E_{tot}(\mathrm{PG+H_2})$ is the total energy of the system, $E_{tot}(\mathrm{PG})$ is the energy of the PG prior to H_2 adsorption, and $E_{tot}(\mathrm{H_2})$ is the total energy of a hydrogen molecule in free space. As in reality hydrogen will be introduced into PG in molecular form, we choose to use H_2 as the reference state. The energy of single atoms is defined to be half the energy of a H_2 molecule.

3. Results and discussion

3.1 *Structure and phonon*

The optimized crystal structures of k the monolayer PG, AB stacked double-layer PG and T12-carbon are shown in Fig. 1. Monolayer PG belongs to the space group $P\bar{4}2_1m$ with two C1 atoms and four C2 atoms per primitive cell, while the symmetries of AB stacked double-layer PG and T12-carbon are given by space group $Cmme$ and $P4_2/ncm$, respectively. Note that the coordination environment of C2 atoms for double-layer PG and T12-carbon is changed, but for ease of comparison, the same label is still used. The calculated structural parameters for three phases are listed in Table 1. The optimized lattice constants of the monolayer PG and T12-carbon agree quite well with the existing theoretical data [1, 22]. The data show that the lattice constant a of these layered carbon allotropies decreases significantly with an increasing number of atomic layers, while the single layer thickness h_1 and layer distance h_2 increase considerably. The obvious variations of the structural parameters may be attributed to stacking-induced changes of the interlayer bonding. This investigation demonstrates the evolution of structural parameters in the covalently bonded layered materials when changing from 3D to 2D regime.

Table 1 - Calculated lattice constants (*a* and *c* in Å), single layer thickness (h_1 in Å), layer distance (h_2 in Å) and cohesive energy per atom(E_c/N in eV/atom) for

monolayer PG, AB stacked double-layer PG and T12-carbon.

Structural	a	c	h_1	h_2	E_c/N
MPG	3.644	-	1.205	-	-7.071
DPG	3.526	-	1.493	3.037	-7.354
TC	3.429	6.091	1.709	3.045	-7.734

Table 1 presents the cohesive energies of the three phases. The cohesive energy of the carbon allotrope is defined as $E_c = E_{\text{total}} - N \times E_{\text{C atom}}$, where E_{total} is the total energy of the allotrope primitive unit cell, N is the number of carbon atoms in the cell and $E_{\text{C atom}}$ is the energy of the isolated carbon atoms. We also calculated the cohesive energies for graphene, diamond, (2, 2) carbon nanotube and C_{20} for comparison. Comparing the cohesive energies of graphene (-7.973 eV/atom), diamond (-7.841 eV/atom), (2, 2) carbon nanotube (-6.873 eV/atom) and C_{20} (-6.833 eV/atom), the monolayer PG, double-layer PG and T12-carbon can also be considered as energetically competitive, though these phases are metastable.

Phonon plays a crucial role in determining the stability of crystal. Figure 2 presents the calculated phonon dispersion curves for monolayer PG, double-layer PG and T12-carbon along the high-symmetry points in the first Brillouin zone (BZ). For monolayer PG, as is a characteristic feature of the phonon dispersion of 2D layered crystals, the out-of-plane acoustical modes (ZA) display parabolic dispersion because the transverse forces decay exponentially, in contrast to the in-plane longitudinal acoustic (LA) and transverse acoustic branches (TA) showing linear dispersions near the Γ point. However, this feature for double-layer PG is not as obvious as that for monolayer PG. From the partial phonon density of states (PDOS) in Fig. 2, the highest-frequency optical phonons at ~ 48 THz dominated by the vibrations of sp^2-hybridized C2 atoms in monolayer and AB stacked double-layer PG disappear in fully sp^3-hybridized T12-carbon. This indicates that the strong interlayer interaction in T12-carbon suppresses C2 atom vibrations. Most importantly, phonon calculations indicate that these phases are dynamically stable, because no imaginary frequencies in the Brillouin zone are found for any of them.

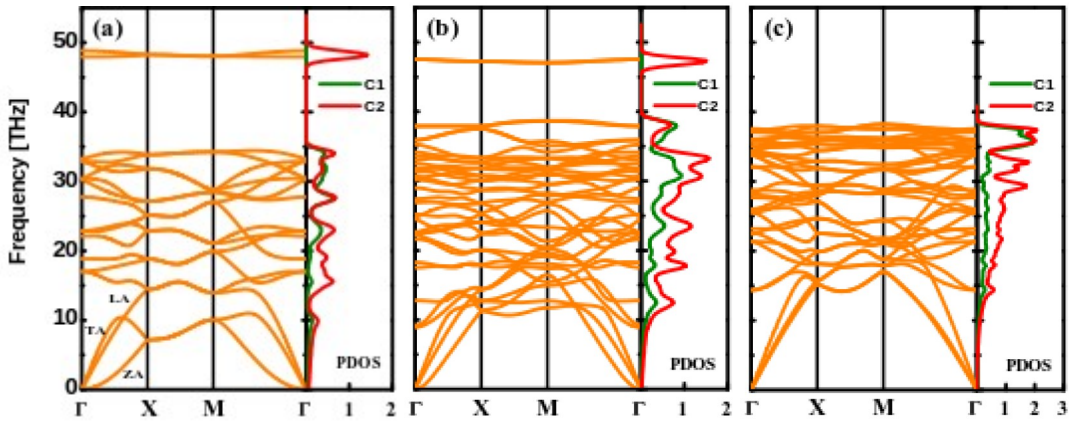

Fig. 2 - *Ab initio* calculation of phonon dispersion curves along the Γ-X-M-Γ directions of the BZ and vibrational partial density of states (PDOS) for monolayer PG, AB stacked double-layer PG and T12-carbon at the equilibrium volume.

3.2 *Electronic properties*

Changes in interlayer interaction and degree of quantum confinement not only result in significant variations of the structural parameters and vibrational properties, but also lead to dramatic differences in the electronic structure of monolayer and double-layer PG compared with their bulk counterpart. This effect has been particularly demonstrated by semiconducting MoS_2. [39] However, compared to the strong covalent bonding between adjacent layers of double-layer PG and T12-carbon, the bulk MoS_2 differs in that the interlayer interactions along the crystallographic *c* axis consist mainly of weak van der Waals forces, stemming from the chemically saturated chalcogen atoms. In order to analyze the electronic properties of 2D monolayer and double-layer PG as well as bulk T12-carbon, their energy band structures are presented in Fig. 3a-d for both HSE06 and GW_0. The solid lines are the HSE06 bands, and the GW_0 bands are given by dotted lines. The Fermi level is shifted to 0 eV. Firstly, we focus on the HSE06 band structures, the bulk T12 phase is an indirect-gap semiconductor having a bandgap of ~4.89 eV with a valence band maximum (VBM) at the Γ point and a conduction band minimum (CBM) at the point along the A-Z symmetry line. As the bulk material transforms to 2D phases, the band gap decreases to ~2.64 eV for double-layer PG and ~3.27 eV for monolayer PG. The double-layer and monolayer PG are also indirect-gap semiconductors whereas the top branches of the valence bands for these 2D phases are very flat. For instance, the value of the valence band at the VB1 point for monolayer PG is very close to that of

VBM. Hence, these 2D phases, especially for the monolayer PG, can be viewed as quasi-direct gap semiconductors.

Intriguingly, the overall features of band structures for the three phases appear quite similar, as can be seen in Fig. 3a-c, except that there are four new bands for the 2D phases located in the original bandgap of T12-carbon. The indirect-to-quasi-direct bandgap transition from bulk to 2D material arises from the four bands in the original bandgap. Consequently, the bandgap becomes much smaller than the bulk material. The transition is manifested in partial charge densities of some selected points near the Fermi level of the three phrases shown in Figs. 3e-g. For T12-carbon, VBM's electronic densities are seen to be primarily localized along the bonds between the C1 and C2 atoms in a single layer, while CBM's electronic densities are mainly localized between two covalently bonded layers. Additionally, the partial charge densities of CB1 appear very similar to that of CBM and are not shown in the figure. Meanwhile, it is worth noting that the partial charge densities of VB1 (CB1) for double-layer PG are also very similar to that of VBM (CBM) in the T12 phase. That is, double-layer PG inherits a portion of the electronic properties from the T12 phase. For monolayer PG, the distribution of partial charge densities for VBM and CBM is dramatically affected by the quantum confinement effect, and is visibly different from that of double-layer PG. However, there are only minor differences between the band structures of the monolayer and double-layer PG.

Compared to the HSE06 results, the GW_0 quasiparticle (QP) correction opens the band gap dramatically by ~1.21 eV for monolayer PG and ~1.03 eV for double-layer PG, while only increases the gap by ~0.30 eV for T12-carbon. It can be also seen that the QP correction is not a simple scissor operation on the HSE06 band structure, there are significant discrepancies in higher lying conduction bands. This emphasizes the importance of using the GW_0 band structure as input for the solution of the BSE to calculate the optical transitions.

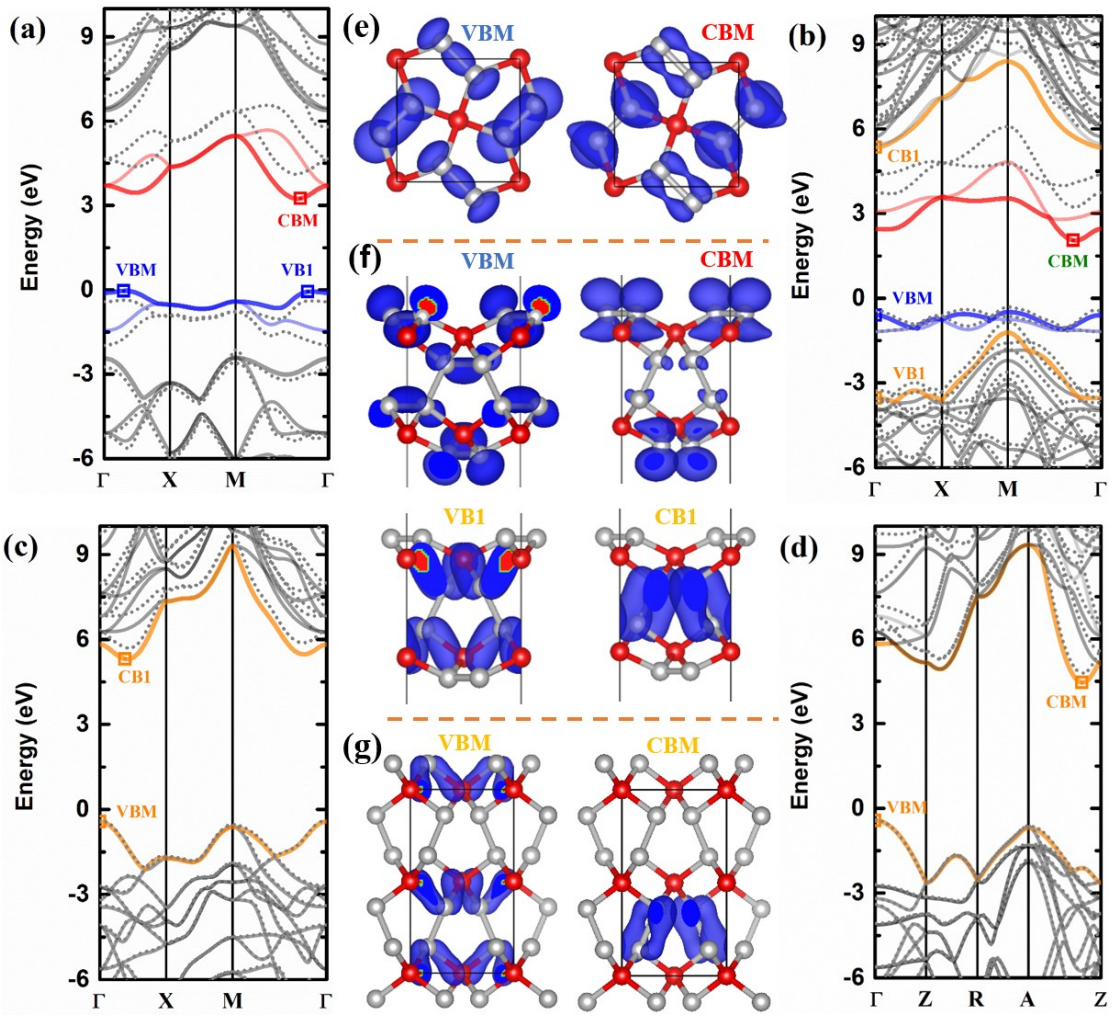

Fig. 3 - Calculated HSE06 (solid lines) and GW0 (dotted lines) band structures of (a) monolayer PG, (b) double-layer PG and (c) T12-carbon along the Γ-X-M-Γ directions of the BZ. (d) Band structure of T12-carbon along the Γ-Z-R-A-Z. Partial charge densities of specific states for (e) monolayer PG, (f) double layer PG and (g) T12-carbon are also shown.

To gain further insight into corresponding electronic structures, the GW_0 total and partial density of states of monolayer PG, double-layer PG and T12-carbon are presented in Fig. 4. The conduction and valence bands of T12-carbon are composed mostly of C1 2*p* and C2 2*p* states. For monolayer and double-layer PG, the lowest conduction bands are mainly attributed to C2 2*p* states, and the top of the valence bands are dominated by hybridizing C2 2*p* and C1 2*p* states.

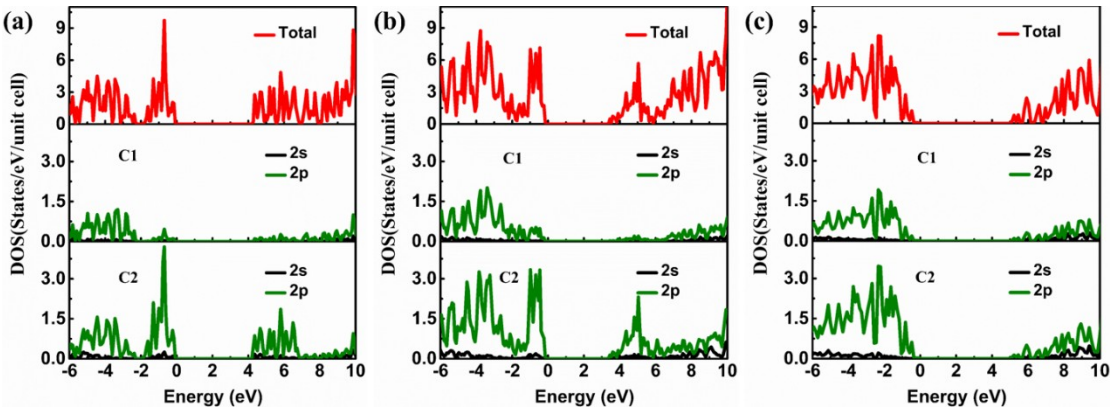

Fig. 4 - Calculated GW_0 partial and total densities of states diagrams for (a) monolayer PG, (b) double layer PG, and (c) T12-carbon.

It is well known that in graphene, the *s*, p_x, and p_y atomic orbitals on each carbon hybridize to form strong covalent sp^2 bonds, and the remaining p_z orbital overlaps with three neighboring carbons to form long-range π-conjugation states, leading to the gapless nature of graphene. Originating from the full sp^3 bonding feature in the T12-carbon, all the *s*, p_x, p_y and p_z atomic orbitals are localized on the sp^3-hybridized C atoms. Thus, the localized states will open a wide bandgap in the T12 phase. Interestingly, monolayer and double-layer PG show a mixed character of graphene and T12-carbon; that is, they exhibit sp^2-sp^3 hybrid carbon structures. Combining the partial charge densities and density of states, the VBM and CBM of monolayer and double-layer PG are dominated by the p_z states of sp^2-hybridized C2 atoms. However, these delocalized states in both 2D structures are spatially separated by the sp^3-hybridized C1 atoms and full electron delocalization is hindered. Accordingly, monolayer and double-layer PG have bandgaps somewhere between graphene and T12-carbon.

3.3 *Optical properties*

We now focus on the optical properties of monolayer PG, double-layer PG and T12-carbon. Fig. 5 shows their real $\varepsilon_1(\omega)$ and imaginary $\varepsilon_2(\omega)$ parts of the dielectric function obtained from BSE calculations on top of QP band structure. For T12-carbon, the dielectric functions are found to be rather featureless, and clearly the onset of obvious absorption is above the fundamental QP band gap and a shoulder is apparent around 10 eV. Our calculations show that in spite of its anisotropic crystal structure T12 carbon exhibits no considerably anisotropic optical response. In the case

of monolayer and double-layer PG, the BSE spectra shows that the onset of absorption is below the QP bang gap due to excitonic effects. Especially, Fig. 5a reveals a pronounced peak near the absorption onset related to an excitonic bound state. And the optical gap of monolayer PG indicated by the first peak of the absorption spectrum is 3.36 eV. The corresponding exciton binding energy defined by the energy difference between the QP band gap and the optical gap is 1.12 eV. Because the surface states for 2D phases are spatially separated by the sp^3-hybridized C1 atoms, the electronic screening is more effective than that in the planar sheet , especially for double-layer PG, resulting in the weaker excitonic effects for double-layer PG.

The origins of the different peaks in the calculated imaginary part of the dielectric function $\varepsilon_2(\omega)$ can be attributed to interband transitions. It is worth mentioning that a particular structural peak in $\varepsilon_2(\omega)$ may correspond to multiple interband transitions since many quasi-direct or indirect transitions may be found in the band structure with an energy corresponding to the same peak. For example, the second peaks for the monolayer and double-layer PG can be mainly assigned to transitions from two valence bands of the four new bands to two conduction bands. According to the analysis of density of states, all the interband transitions for the three phases are mainly due to transitions from 2*p* of C2 to the 2*p* of C2. The contributions from transitions from 2*p* of C1 to the 2*p* of C2 as well as 2*p* of C2 to the 2*p* of C1 are also very large for the high-energy peaks. Considering the selection rules, only transitions with the difference $\Delta l = \pm 1$ between the angular momentum quantum numbers l are allowed, i.e., the atomic *p*-*p* transition is forbidden. However, in the three phases, due to the orbital hybridization, the valence and conduction bands still have 2*s* orbital contributions; thus the transition dominated by the 2*p*-2*p* transition is still allowed.

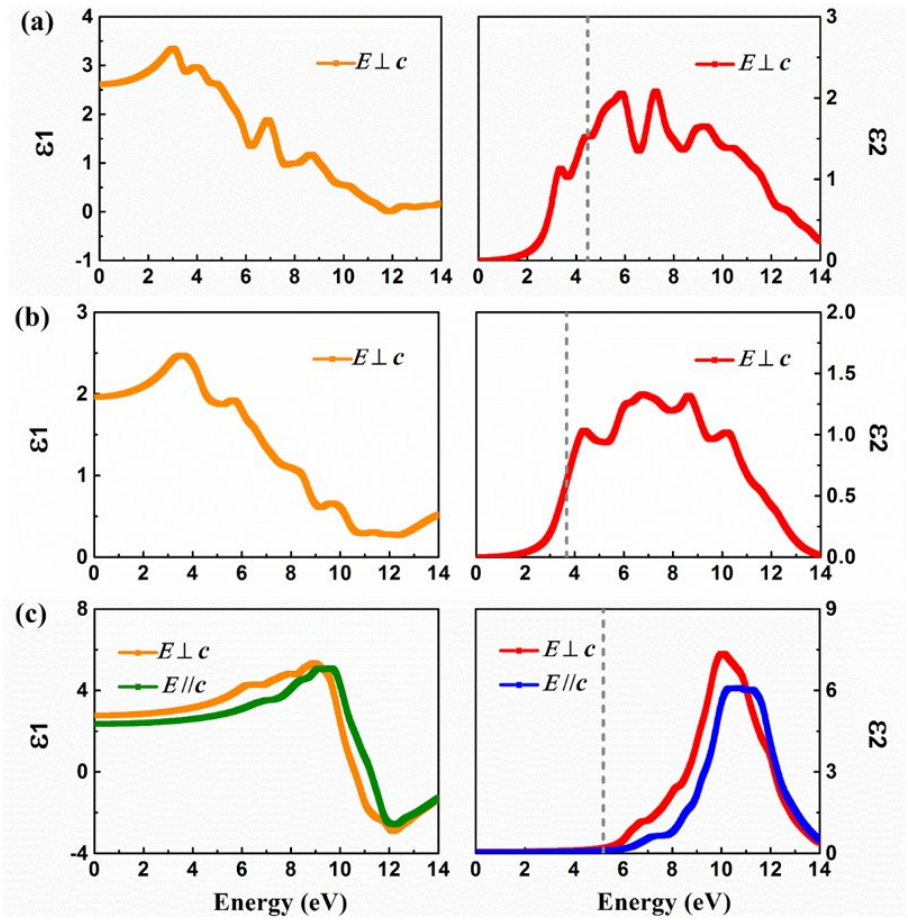

Fig. 5 - Calculated real $\varepsilon_1(\omega)$ and imaginary $\varepsilon_2(\omega)$ parts of the dielectric function versus photon energy of (a) the monolayer PG, (b) double-layer PG and (c) T12 predicted using BSE on top of GW_0. The dotted lines in the right panel indicate the GW_0 band gaps.

Figure 6a-c depicts the calculated results for refractive index, extinction coefficient, absorption spectrum, reflectivity, and energy loss spectrum for monolayer PG, double-layer PG and T12-carbon, respectively. For the $E \perp c$ of monolayer PG, double-layer PG and T12-carbon, the static refractive index is found to have a value of 1.62, 1.40 and 1.66, respectively. For T12-carbon, the refractive index reaches a maximum value of 2.48 at 9.50 eV. Strong absorption is found above ~8 eV for T12-carbon. For the 2D phases, strong absorption is also found above ~3 eV.

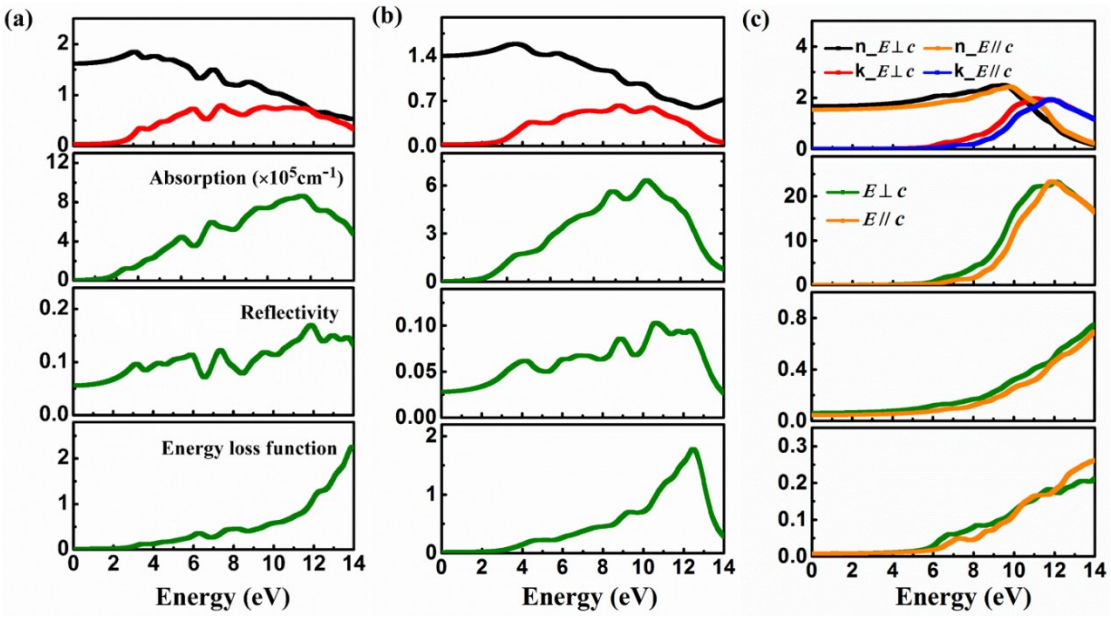

Fig. 6 - Calculated refractive index n, extinction coefficient k, absorption spectrum, reflectivity, and energy-loss spectrum for (a) monolayer PG, (b) double-layer PG and (c) T12.

3.3 *Chemical stability*

As a versatile material, it seems inevitable to use PG-based devices in various chemical environments. In the chemical exfoliation procedure to synthesize a monolayer PG, the exfoliated carbon layers may be hydrogenated by exposing to hydrogen atmosphere. Due to the prohibitive computational cost, we only choose the hydrogenation of monolayer PG as a prototypical example to study the chemical stability of these carbon allotropes.

First, we studied the H_2 dissociation on the monolayer PG. Two pathways are considered as shown in Fig. 7a, together with the top views of the involved structures in these reactions. In first pathway denoted as path I, H_2 molecule along the C2–C2 bond is chosen as the initial state, and H_2 above the C1 atom is chosen in the second pathway denoted as path II. In both adsorption state, H_2 lies parallel to the sheet and the optimized distance between the sheet and the closest H atom is 4.01 Å for path I and 3.45 Å for path II. There is almost no preference for the H_2 being above the C2–C2 bond or the C1 atom. The adsorption energy is only several meV/H_2. In the path I, the dissociation is ended up with two H atoms on two bonded C2 atoms with an adsorption energy of -2.70 eV/H_2, and the whole process is exothermic. This barrier for H_2 to 2H dissociation in this path with a rather high value of 2.18 eV, is a

bit lower than that of graphene (2.95 eV). There is a significant barrier of height 4.88 eV preventing chemisorbed hydrogen association to H_2. In the case of the path II, the adsorption energy for the final state is only -0.45 eV/H_2. The H_2 dissociation energy is 0.58 eV lower than the barrier in path I. The barrier for hydrogen dissociation away from the sheet is much lower than that in path I, but the value is still large than 2.0 eV. Therefore, it is not easy for the H_2 molecule to dissociate on the monolayer PG, and the chemisorbed H dissociation away from the sheet is much more difficult.

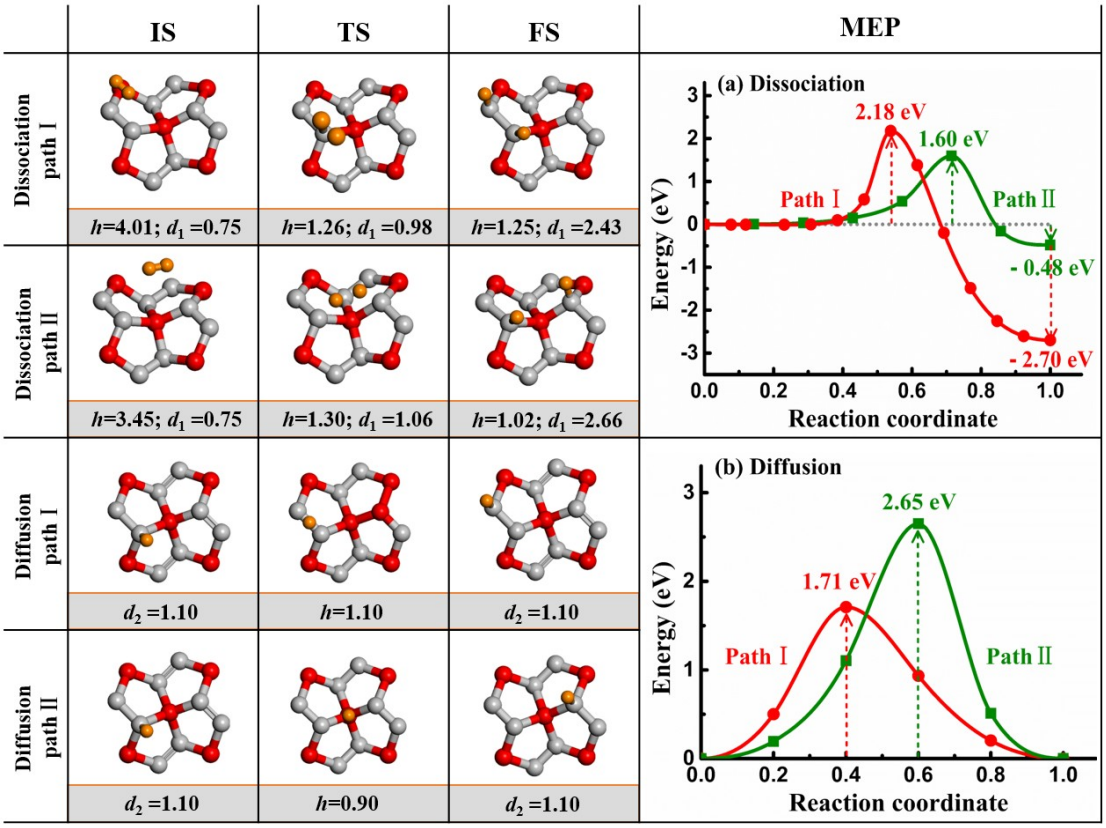

Fig. 7 - Calculated reaction diagrams of (a) H_2 dissociation along path I and path II, and (b) H diffusion along path I and path II. The energy of IS states is set to be zero. The schematic diagrams of initial (IS), transition (TS), and final (FS) states involved in the reactions as well as the distance between the sheet and the closest H atom *h* (Å), H–H distance d_1 (Å) and C–H bond length d_2 (Å) are illustrated in left panel (H, orange; C1, red; C2, grey).

We have also investigated the mobility of a single H atom along the C2-C2 (path I) and C2-C1-C2 (path II) paths on monolayer PG. The reaction diagram of each diffusion process is plotted in Fig. 7b, together with the top views of the involved structures in these reactions. The adsorption energy for isolated H directly adsorbed

on C2 atom is -0.24 eV/H(H_2), the hydrogenation strength is much stronger than that of 1.51 eV/H(H_2) for hydrogenated graphene. The calculated diffusion barriers by considering the minimum energy path indicate that both migration barriers are significantly larger than that of graphene (0.95 eV), making the diffusion of hydrogen on monolayer PG is highly unfavorable.

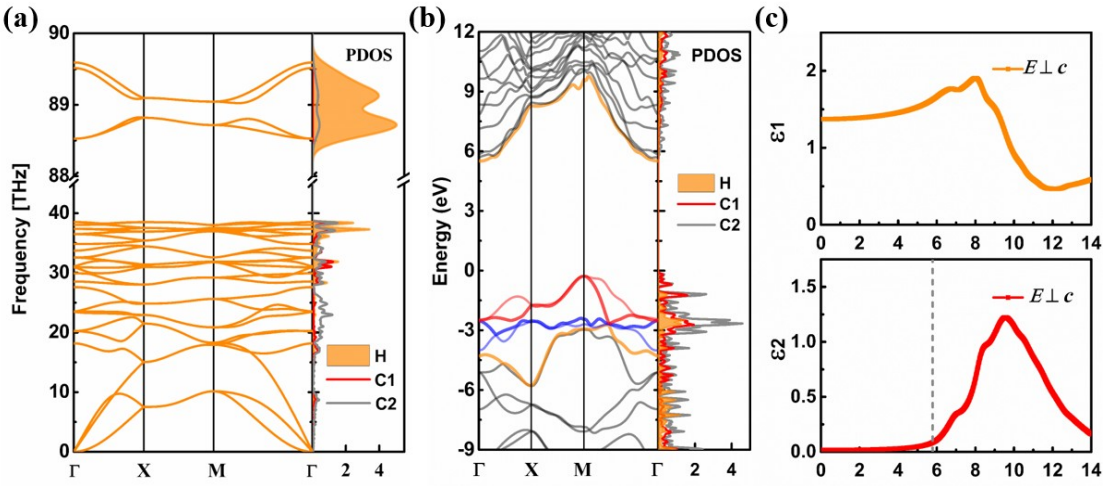

Fig. 8 - Calculated (a) phonon band structure and vibrational partial density of states, (b) GW_0 electronic band structure and partial densities of states, and (c) BSE real $\varepsilon_1(\omega)$ and imaginary $\varepsilon_2(\omega)$ parts of the dielectric function for double-side hydrogenated monolayer PG.

Apart from the negative consequences due to the interaction with impurities, a controlled passivation of PG might lead to new stable structures as it shows the prominent example of graphene derivatives. Considering the chemical stability of hydrogenated PG, we study the phonon spectra, electronic, and optical properties of double-side hydrogenated monolayer PG using first-principles calculations. As shown in Fig. 8, hydrogenated monolayer PG is dynamically stable, and H atoms have rather high vibrational frequencies of ~89 and 38 THz. The GW_0 calculations show that hydrogenated monolayer PG is an indirect-gap semiconductor having a large bandgap of ~5.78 eV with a valence band maximum near the Γ point and a conduction band minimum at the M point. The four new bands for the 2D phases drop into the conduction bands and become the new conduction band edge. Furthermore, the passivation of H atoms dramatically changes the optical properties of monolayer PG, the optical absorption edge shifts noticeably upward, and the excitonic contributions are very small.

4. Conclusions

In summary, first principles calculations have been performed to obtain the structure as well as the phonon spectra, electronic and optical properties of monolayer PG, AB stacked double-layer PG and T12-carbon. The optimized lattice constants of the monolayer PG and T12-carbon agree quite well with the available theoretical data. These carbon allotropes have slightly higher cohesive energies than graphene and diamond, and are also energetically favorable. Phonon calculations indicate that the three phases are dynamically stable. The bulk T12 phase is an indirect-gap semiconductor having a QP bandgap of ~5.19 eV, whereas the double-layer and monolayer PG become quasi-direct gap semiconductors with the band gap decreasing to ~3.67 eV for double-layer PG and ~4.48 eV for monolayer PG. The indirect-to-quasi-direct bandgap transition arises from the four new bands in the original bandgap. Meanwhile, monolayer and double-layer PG inherit the main band structure features from the T12 phase. The linear photon energy dependent complex dielectric functions and related optical properties including refractive index, extinction coefficient, absorption spectrum, reflectivity, and energy loss spectrum were computed and discussed. Additionally, the chemical stability of monolayer PG and the electronic and optical properties of double-side hydrogenated monolayer PG were also studied. Our investigations are beneficial to the practical applications of these exotic carbon allotropes in optoelectronics and electronics.

Acknowledgments

W. S. Su would like to thank the Ministry of Science and Technology for financially supporting this research under Contract No. MOST-104-2112-M-492-001. Support from the National Centers for Theoretical Sciences and High-performance Computing of Taiwan in providing significant computing resources to facilitate this research are also gratefully acknowledged. Work at Fudan University was supported by the NSF of China (Grant No. 11374055 and 61427815), and National Basic Research Program of China (No. 2012CB934303 and 2010CB933703). Work at Ames Laboratory was supported by the US Department of Energy, Basic Energy Sciences, and Division of Materials Science and Engineering, including a grant of computer time at the National Energy Research Scientific Computing Centre (NERSC) in Berkeley, CA under Contract No. DE-AC02-07CH11358.

References

[1] Zhang S, Zhou J, Wang Q, Chen X, Kawazoe Y, Jena P. Penta-graphene: A new carbon allotrope. Proc Natl Acad Sci USA. 2015;112(8):2372-7.

[2] Gupta A, Sakthivel T, Seal S. Recent development in 2D materials beyond graphene. Prog Mater Sci. 2015;73:44-126.

[3] Butler SZ, Hollen SM, Cao L, Cui Y, Gupta JA, Gutierrez HR, et al. Progress, challenges, and opportunities in two-dimensional materials beyond graphene. ACS nano. 2013;7(4):2898-926.

[4] Coleman JN, Lotya M, O'Neill A, Bergin SD, King PJ, Khan U, et al. Two-dimensional nanosheets produced by liquid exfoliation of layered materials. Science. 2011;331(6017):568-71.

[5] Allen MJ, Tung VC, Kaner RB. Honeycomb carbon: a review of graphene. Chemical reviews. 2010;110(1):132-45.

[6] Mas-Balleste R, Gomez-Navarro C, Gomez-Herrero J, Zamora F. 2D materials: to graphene and beyond. Nanoscale. 2011;3(1):20-30.

[7] Lin Y, Connell JW. Advances in 2D boron nitride nanostructures: nanosheets, nanoribbons, nanomeshes, and hybrids with graphene. Nanoscale. 2012;4(22):6908-39.

[8] Gibney E. 2D OR NOT 2D. Nature. 2015;522(7556):274-6.

[9] Davila ME, Xian L, Cahangirov S, Rubio A, Le Lay G. Germanene: a novel two-dimensional germanium allotrope akin to graphene and silicene. New J Phys. 2014;16:095002.

[10] Liu H, Neal AT, Zhu Z, Luo Z, Xu X, Tomanek D, et al. Phosphorene: An Unexplored 2D Semiconductor with a High Hole Mobility. ACS nano. 2014;8(4):4033-41.

[11] Osada M, Sasaki T. Two-dimensional dielectric nanosheets: novel nanoelectronics from nanocrystal building blocks. Advanced materials. 2012;24(2):210-28.

[12] Xu M, Liang T, Shi M, Chen H. Graphene-like two-dimensional materials. Chemical reviews. 2013;113(5):3766-98.

[13] Yagmurcukardes M, Sahin H, Kang J, Torun E, Peeters FM, Senger RT. Pentagonal monolayer crystals of carbon, boron nitride, and silver azide. Journal of Applied Physics. 2015;118(10):104303.

[14] Cranford SW. When is 6 less than 5? Penta- to hexa-graphene transition. Carbon. 2016;96:421-8.

[15] Kannan PK, Late DJ, Morgan H, Rout CS. Recent developments in 2D layered inorganic nanomaterials for sensing. Nanoscale. 2015;7(32):13293-312.

[16] Das SR, Kwon J, Prakash A, Delker CJ, Das S, Janes DB. Low-frequency noise in MoSe2 field effect transistors. Appl Phys Lett. 2015;106(8):083507.

[17] Huo N, Kang J, Wei Z, Li S-S, Li J, Wei S-H. Novel and Enhanced Optoelectronic Performances of Multilayer MoS2-WS2 Heterostructure Transistors. Adv Funct Mater. 2014;24(44):7025-31.

[18] Wang H, Yuan X, Zeng G, Wu Y, Liu Y, Jiang Q, et al. Three dimensional graphene based materials: Synthesis and applications from energy storage and conversion to electrochemical sensor and environmental remediation. Adv Colloid Interface Sci. 2015;221:41-59.

[19] Schwierz F. Graphene transistors. Nature Nanotech. 2010;5(7):487-96.

[20] Ferrari AC, Bonaccorso F, Fal'ko V, Novoselov KS, Roche S, Boggild P, et al. Science and technology roadmap for graphene, related two-dimensional crystals, and hybrid systems. Nanoscale. 2015;7(11):4598-810.

[21] Deza M, Fowler PW, Shtogrin M, Vietze K. Pentaheptite modifications of the

graphite sheet. Journal of chemical information and computer sciences. 2000;40(6):1325-32.
[22] Zhao Z, Tian F, Dong X, Li Q, Wang Q, Wang H, et al. Tetragonal Allotrope of Group 14 Elements. J Am Chem Soc. 2012;134(30):12362-5.
[23] Yu ZG, Zhang Y-W. A comparative density functional study on electrical properties of layered penta-graphene. Journal of Applied Physics. 2015;118(16):165706.
[24] Xu W, Zhang G, Li B. Thermal conductivity of penta-graphene from molecular dynamics study. The Journal of chemical physics. 2015;143(15):154703.
[25] Chuang C, Fan YC, Jin BY. Procedia Engineering. 2011;4: 2373-58.
[26] Kresse G, Joubert D. From ultrasoft pseudopotentials to the projector augmented-wave method. Phys Rev B. 1999;59(3):1758-75.
[27] Kresse G, Furthmüller J. Efficient iterative schemes for ab initio total-energy calculations using a plane-wave basis set. Phys Rev B. 1996;54(16):11169-86.
[28] Kresse G, Furthmüller J. Efficiency of ab-initio total energy calculations for metals and semiconductors using a plane-wave basis set. Comp Mater Sci. 1996;6(1):15-50.
[29] Blöchl PE. Projector augmented-wave method. Phys Rev B. 1994;50(24):17953-79.
[30] Perdew JP, Burke K, Ernzerhof M. Generalized gradient approximation made simple. Phys Rev Lett. 1996;77(18):3865-8.
[31] Monkhorst HJ, Pack JD. SPECIAL POINTS FOR BRILLOUIN-ZONE INTEGRATIONS. Phys Rev B. 1976;13(12):5188-92.
[32] Togo A, Oba F, Tanaka I. First-principles calculations of the ferroelastic transition between rutile-type and CaCl(2)-type SiO(2) at high pressures. Phys Rev B. 2008;78(13):134106.
[33] Heyd J, Scuseria GE, Ernzerhof M. Hybrid functionals based on a screened Coulomb potential. J Chem Phys. 2003;118(18):8207-15.
[34] Heyd J, Scuseria GE, Ernzerhof M. Hybrid functionals based on a screened Coulomb potential (vol 118, pg 8207, 2003). J Chem Phys. 2006;124(21):219906.
[35] Onida G, Reining L, Rubio A. Electronic excitations: density-functional versus many-body Green's-function approaches. Reviews of Modern Physics. 2002;74(2):601-59.
[36] Mostofi AA, Yates JR, Lee Y-S, Souza I, Vanderbilt D, Marzari N. wannier90: A tool for obtaining maximally-localised Wannier functions. Computer Physics Communications. 2008;178(9):685-99.
[37] Henkelman G, Jónsson H. Improved tangent estimate in the nudged elastic band method for finding minimum energy paths and saddle points. The Journal of chemical physics. 2000;113(22):9978.
[38] Henkelman G, Uberuaga BP, Jónsson H. A climbing image nudged elastic band method for finding saddle points and minimum energy paths. The Journal of chemical physics. 2000;113(22):9901.
[39] Mak KF, Lee C, Hone J, Shan J, Heinz TF. Atomically Thin MoS2: A New Direct-Gap Semiconductor. Physical Review Letters. 2010;105(13):136805.